

Atomtronic multi-terminal Aharonov-Bohm interferometer

Jonathan Wei Zhong Lau,^{1,*} Koon Siang Gan,¹ Rainer Dumke,^{1,2}
Luigi Amico,^{1,3,4,5,†} Leong-Chuan Kwek,^{1,6,7,8} and Tobias Haug^{9,‡}

¹Centre for Quantum Technologies, National University of Singapore 117543, Singapore

²School of Physical and Mathematical Sciences, Nanyang Technological University 637371, Singapore

³Quantum Research Centre, Technology Innovation Institute, Abu Dhabi, UAE

⁴INFN-Sezione di Catania, Via S. Sofia 64, 95127 Catania, Italy

⁵LANEF 'Chaire d'excellence', Université Grenoble-Alpes & CNRS, F-38000 Grenoble, France

⁶MajuLab, CNRS-UNS-NUS-NTU International Joint Research Unit, UMI 3654, Singapore

⁷National Institute of Education, Nanyang Technological University, 1 Nanyang Walk, Singapore 637616

⁸School of Electrical and Electronic Engineering Block S2.1, 50 Nanyang Avenue, Singapore 639798

⁹QOLS, Blackett Laboratory, Imperial College London SW7 2AZ, UK

(Dated: July 13, 2022)

We study a multi-functional device for cold atoms consisting of a three-terminal ring circuit pierced by a synthetic magnetic flux. The flux controls the atomic current through the ring via the Aharonov-Bohm effect. Our device can measure the flux in-situ via a flux-induced transition of the reflections from an Andreev-like negative density to positive density. In the non-equilibrium regime, the flux directs the atomic current into specific output ports, realizing a flexible non-reciprocal switch to connect multiple atomic systems. By changing the flux linearly in time, we convert constant matter wave currents into alternating currents. This effect can be used to realize an atomic frequency generator and study fundamental problems related to the Aharonov-Bohm effect. We demonstrate the viability of the setup by loading a Bose-Einstein condensate into a light-shaped optical potential of the three-terminal ring. Our work opens up novel atomtronic devices for practical applications in quantum technologies.

Precise control over quantum systems has led to the rapid development of quantum technologies for applications in quantum simulation [1], quantum communication [2] and metrology [3]. These latter fields are fundamental to atomtronics [4], an emerging quantum technology of propagating cold atoms within matter-wave circuits [3–5]. Inspired originally by electronics, atomtronics exploits the advancement in optical traps and cooling together with this precision control to move coherent ultracold atoms in optical traps and waveguides. Such transports realize novel and practical quantum devices [6–9]. Indeed, simple atomtronic circuits loaded with Bose-Einstein condensates (BECs) or degenerate fermions that mimick classical transports have already exhibited new physics with novel potential applications [10–22].

The construction of feasible atomtronic circuits requires an in-depth understanding of the transport of cold atom matter. Such studies, both theoretically and experimentally, have blossomed in recent years [1, 16, 23–28]. Analogues of one-dimensional mesoscopic conductors are also investigated [29–33] with transport now possible over macroscopic distances [34]. In particular, BECs trapped in ring shaped potentials [35–38] and Y-shaped junctions [7, 39, 40] augurs potential practical applications due in part to its subtle similarity to integrated photonic chips. However, such systems exhibit superfluid current flows [20, 41–43] and realize effective two-level dynamics for a potential atomtronic qubit [44, 45].

A promising geometry for cold atom devices is the ring-shaped circuit. Here, the transport can be con-

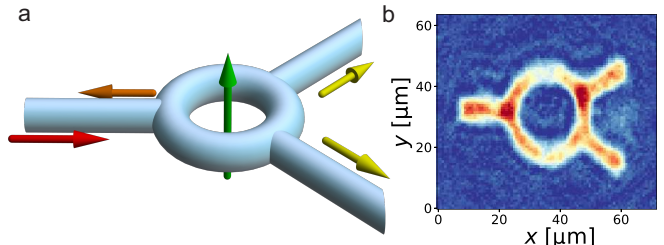


FIG. 1. **a)** Three-terminal Aharonov-Bohm circuit with source lead (left) attached to a ring with two drain leads (right). A synthetic Aharonov-Bohm flux Ω through the ring controls the current flowing from source to the drains, which can be used for multiple functionalities. **b)** An initial experimental demonstration of the setup with a BEC. $6 \cdot 10^4$ Rubidium atoms are cooled to 50 nK by atom evaporation into an optical potential created by a digital micromirror device. We show the *in-situ* atomic density measured with absorption imaging.

trolled by the Aharonov-Bohm effect where the magnetic flux changes the interference of matter [46]. In mesoscopic electronic rings, the Aharonov-Bohm effect controls the conductance [47–50]. An open theoretical and experimental question is whether a time-dependent magnetic field produces an Aharonov-Bohm effect [51–54]. Through the application of suitable synthetic fields [19, 20, 55–59], cold atoms can harness the Aharonov-Bohm effect with a high degree of control and coherence that is difficult to reach in other systems. An important example is the transport through two-terminal Aharonov-Bohm

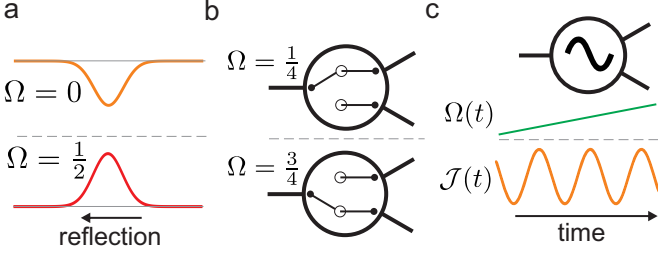


FIG. 2. Applications of three-terminal cold atom Aharonov-Bohm circuit. **a)** Rotation sensing by monitoring reflection of density waves changes from negative (Andreev-like) to positive with flux Ω . **b)** Directional switch of the current to one of the output terminals by adjusting Ω . **c)** Atomic frequency generator or a DC/AC converter with a sinusoidal output current $J(t)$ of period T by linearly increasing $\Omega(t) = t/T$ in time.

rings with bosonic atoms [37, 39, 40].

Here, we study the transport in a three terminal circuit in which a bosonic condensate is guided from a source lead through a Aharonov-Bohm ring attached to two drains - see Fig.1a. The setup is fabricated by loading a Bose-Einstein condensate (BEC) of ^{78}Rb atoms in a Digital Micromirror Device (DMD) generated optical potential - see Fig.1b. We demonstrate that our scheme provides a novel concept for a multi-functional device: the system can (i) sense rotation; (ii) realize a non-reciprocal switch; (iii) convert direct current (DC) into alternating current (AC) matter-waves.

We first introduce the system together with an experimental demonstration of the setup. We then analyze the low energy and highly non-equilibrium dynamics of the system as well as the dynamics under a time-dependent driving of the flux. We highlight the three functionalities of our device in the discussion section and in Fig.2.

Model.— A sketch of the three-terminal ring pierced by flux Ω is shown in Fig. 1a. We experimentally demonstrate the feasibility of the setup by loading a BEC into a static optical potential generated by a Digital Micromirror Device (see Fig. 1b and the Supplemental Material (SM) E for details). We simulate the system numerically with the Bose-Hubbard model by dividing the system into the source lead, two drain leads and the ring with L sites. The source lead s and the two drains b, c are connected to the ring in a symmetric manner with $x_s = 1$, $x_b = L/3$ and $x_c = 2L/3$. The system Hamiltonian

$H = H_r + H_\ell + H_{r\ell}$ with N bosons is given by

$$H_r = \sum_{j=1}^L \left[\frac{U}{2} \hat{n}_j (\hat{n}_j - 1) - J(e^{-i2\pi\Omega(t)/L} \hat{a}_{j+1}^\dagger \hat{a}_j + H.C.) \right]$$

$$H_{r\ell} = -K \sum_{\alpha=\{b,c,s\}} \left(\hat{a}_1^\dagger \hat{a}_{x_\alpha} + H.C. \right) \quad (1)$$

$$H_\ell = \sum_{\alpha=\{b,c,s\}} \sum_{j=1}^{L_\alpha} \left[\frac{U_\alpha}{2} \hat{n}_j^\alpha (\hat{n}_j^\alpha - 1) - J_\alpha (\hat{a}_{j+1}^\dagger \hat{a}_j + H.C.) \right]$$

where $\hat{a}_j (\hat{a}_j^\dagger)$ is the bosonic annihilation (creation) operator at site j on the ring, and $\hat{n}_j = \hat{a}_j^\dagger \hat{a}_j$ is the corresponding number operator. We impose periodic boundary conditions in the ring with $\hat{a}_{L+1} = \hat{a}_1$. $\Omega(t)$ represents the total flux through the ring which can be dependent on time t . This flux can be generated for neutral atoms via rotation, where the Coriolis flux mimics the effect of the magnetic field [20, 60]. This can be achieved by stirring the ring with angular frequency $\omega = \frac{\Omega h}{mR^2}$, where m is the atom mass and R the radius of the ring, yielding for the parameters of Fig.1b $\omega = 5.1\Omega\text{Hz}$ [35]. Alternatively, synthetic magnetic fields can be achieved by counter-propagating Raman beams [56, 57] or driving the optical potential in time [61].

Due to flux quantization in the ring, the spectrum of $H(\Omega)$ is periodic with $\Omega \rightarrow \Omega + k$, k being integer, with the flux quantum set to 1. J is the intra-ring coupling strength and U the interaction strength of the ring. \hat{a}_j is the annihilation operator, \hat{n}_j^α the number operator, L_α the number of sites, U_α the interaction strength and J_α the intra-reservoir couplings for the source and drains with $\alpha \in \{s, b, c\}$. The current operator between lead α and ring is given by

$$J_\alpha = -iK(\hat{a}_1^\dagger \hat{a}_{x_\alpha} - H.C.). \quad (2)$$

The continuous circuit realized experimentally in Fig.1 corresponds to a lattice Hamiltonian (1) in the dilute limit of small filling fractions N/L .

Low-energy dynamics.— First, we study the dynamics close to the ground state as a function of the flux Ω . We add a perturbation Hamiltonian with the local potential acting on the sites of the source Hamiltonian $H_e = -\epsilon_s \sum_{j=1}^{L_s} \exp[-(j-D)^2/2\sigma^2] \hat{n}_j^s$ with $D = L_s/2$, $\sigma = 2$ and $\epsilon_s = 0.3$. We first prepare the ground state of the Hamiltonian $H + H_e$. The ground state has a slightly raised density in the source on the sites where H_e is acting on. At $t > 0$ we switch off H_e and evolve the system only with Hamiltonian H . The raised density starts to move in both positive and negative direction as a density wave (the packet in the negative direction can be ignored for a sufficiently large source lead). We investigate the change in density $\Delta n(t) = \langle n(t) \rangle - n_0$ in time, where n_0 is the average density of the total system. The dynamics is calculated using matrix product states with

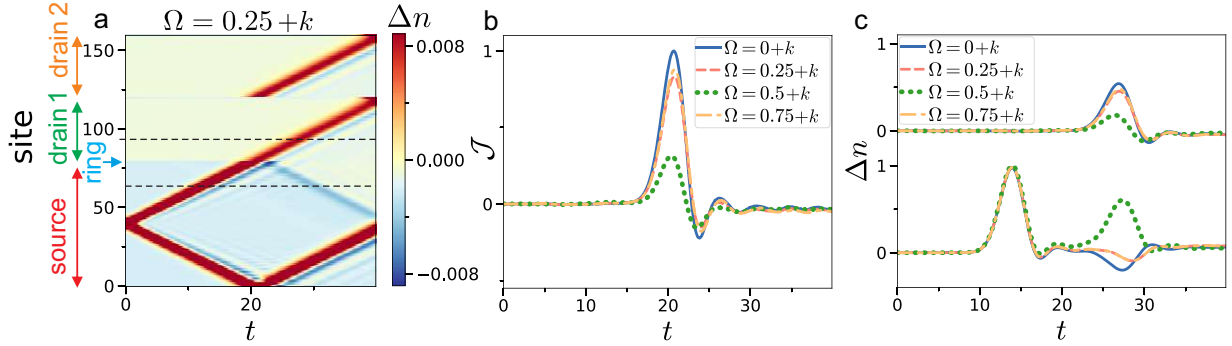


FIG. 3. Dynamics of low-energy excitations in three-terminal ring device. **a)** Change of density relative to average density $\Delta n(t) = \langle n(t) \rangle - n_0$ as function of time and sites of source, ring, drain 1 and 2 for $\Omega = \frac{1}{4} + k$, where k is an integer. The density wave moves both forward and backward. The forward propagating wave is transmitted into the drains, as well as reflected back into the source. Note that the dynamics in both drains is nearly symmetric for all values of flux. **b)** Current \mathcal{J} into the first drain against time and Ω . **c)** Δn in source (bottom) and first drain (top) measured at positions shown as dashed lines in a). At $t = 27$ in the bottom curve, the reflected density wave is seen with positive or negative amplitude depending on Ω . We have hard-core bosons with $J = 1$, $K = 0.5$ and in total $L = 160$ lattice sites and $N = 80$ bosons ($L = 3$, $L_s = 79$, $L_b = L_c = 39$).

the ITensor library [62]. In Fig.3a we show the dynamics of $\Delta n(t)$ for $\Omega = \frac{1}{4} + k$, k being integer, as function of time t and the sites of source, ring and drain (see SM B for other values of Ω). We find that the forward propagating density wave moves from the source to the ring, then is transmitted into the drains as well as reflected back to the source. For any value of Ω we find that the transmission into drain 1 and drain 2 is nearly the same. The magnitude of the current \mathcal{J} into the first drain is shown in Fig.3b. The current is maximal for $\Omega = k$ and minimal for $\Omega = \frac{1}{2} + k$. We find nearly the same current for $\Omega = \frac{1}{4} + k$ and $\Omega = \frac{3}{4} + k$, which is the result of an emergent reflection symmetry $\Omega \rightarrow -\Omega$. We show the density Δn at a fixed site in source and drain in Fig.3c. We find that the reflection into the source at a specific time t_r ($t_r \sim 27$ in Fig.3c) changes in nature with Ω . For $\Omega = k$ we find a clear negative reflection, which is a hallmark of Andreev reflections. With increasing Ω , the Andreev reflections turn into positive reflections. Similar results to the matrix product state can be obtained by alternatively simulating the system with a Gross-Pitaevskii equation, which is known to be accurate for the limit of dilute gases and large site numbers.

Dynamics far from ground state.— We investigate the dynamics when the system is far from the ground state. We apply a quench protocol. The ring and drains are initially empty, and then the ring is coupled to the source lead filled with atoms, which injects atoms into the ring. We study this highly non-equilibrium setting in the limits of zero and infinite interaction in the following.

In the limit of zero interaction $U = 0$, we describe the dynamics with the Landauer formalism as explained in

SM A, which yields a transmission of

$$G_\alpha = 16 \left| \frac{1 - \sqrt{2} + 2i(2\sqrt{2} - 3) \exp(-i\pi(2\Omega + \alpha))}{62 - 46\sqrt{2} + 2i \cos(\pi(2\Omega + \alpha))} \right|^2 \quad (3)$$

into the respective drains $\alpha \in \{1, 2\}$. The resulting transmission and reflection of the system is shown in Fig.4a. In contrast to the dynamics close to the ground state, the symmetry with Ω between the drains is broken. As a result, for $\Omega = \frac{1}{4}$ we have unit transmission into drain 1, and zero transmission into drain 2. For $\Omega = \frac{3}{4}$ the dynamics of the drains is interchanged, with maximal transmission into drain 2 and zero into drain 1. Thus, we can direct the all of the current either into drain 1 or drain 2, realizing a perfect non-reciprocal switch with zero back-reflection.

Next, we investigate the limit of strong interaction with hard-core bosons, where each site occupies at most one boson. We further simplify the source and drain leads by tracing out all of their sites except the very first one coupled to the ring (\hat{s}_1 , \hat{b}_1 and \hat{c}_1). The effect of the reservoirs on the reduced density matrix ρ within the Born-Markov approximation is encapsulated by Lindblad operators L_m [39, 63]

$$\frac{\partial \rho}{\partial t} = -\frac{i}{\hbar} [H, \rho] - \frac{1}{2} \sum_m \{L_m^\dagger L_m, \rho\} + \sum_m L_m \rho L_m^\dagger \quad (4)$$

with the dissipators $L_1 = B_s \hat{s}_1^\dagger$, $L_2 = B_b \hat{b}_1$, $L_3 = B_c \hat{c}_1$ and dissipator strength B_α . L_1 describes bosons entering the system at the source site, and L_2 , L_3 atoms leaving to the respective drains. We solve for the steady-state ρ_{ss} via $\partial \rho_{ss} / \partial t = 0$ [64]. In Fig.4b we show the steady-state current through source and drains as function of flux Ω . The current in drain 1 and 2 varies strongly with Ω , allowing for directional control into either drain

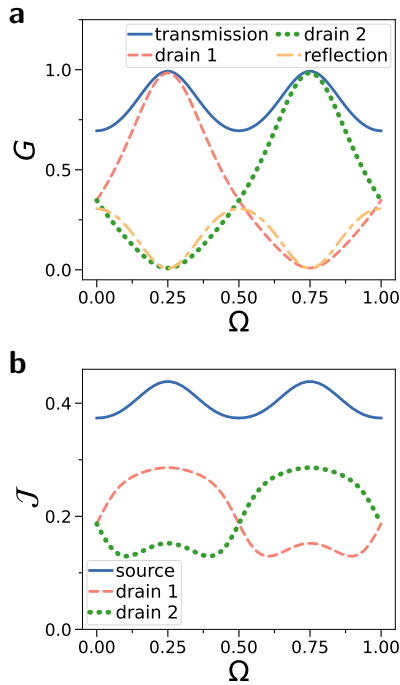


FIG. 4. Transport through three-terminal device for non-equilibrium setting as function of flux Ω . **a)** Landauer formalism for three-terminal ring device for non-interacting bosons. We show the total transmission and reflection of the system, as well as the transmission into drain 1 and 2 as function of flux Ω . **b)** Steady-state current J for hard-core bosons as function of flux Ω for $J = 1$, $L = 3$, $K = 1$ and $B_s = B_d = 1$.

similar to the non-interacting case. The source current changes from being flux-independent to flux-dependent with intra-ring coupling J (see SM C).

Time-dependent flux.— The flux $\Omega(t) = t/T$ is then linearly increased in time, where we increase by one flux quantum in one period T . As a result, the current undergoes a periodic modulation. For $t > 0$, we inject atoms via the source into the initially empty ring and drains. We show the case of $T = 2.8$ in Fig. 5a. The current undergoes an initial transient until it settles into periodic sinusoidal oscillations. The drain current is shifted by $T/2$, i.e. when one of the drains has minimal current, the other drain has maximal current. The drain current oscillates between close to 0 and the magnitude of the source current. Thus, this device realizes an atomic DC/AC converter where a constant source current is converted into an alternating current. For an optimal conversion, we want the amplitude of the drain current oscillation to be as close as possible to the incoming source current.

We investigate the conversion efficiency $C = \Delta\mathcal{J}_{\text{drain}}/\langle\mathcal{J}_{\text{source}}\rangle$ of the DC/AC converter as function of T and J in Fig. 5b. We define the drain current amplitude $\Delta\mathcal{J}_{\text{drain}} = \max_{t/T \gg 1} \mathcal{J}_{\text{drain}}(t) - \min_{t/T \gg 1} \mathcal{J}_{\text{drain}}(t)$ and the mean source current $\langle\mathcal{J}_{\text{source}}\rangle = \text{mean}_{t/T \gg 1} \mathcal{J}_{\text{source}}(t)$, where

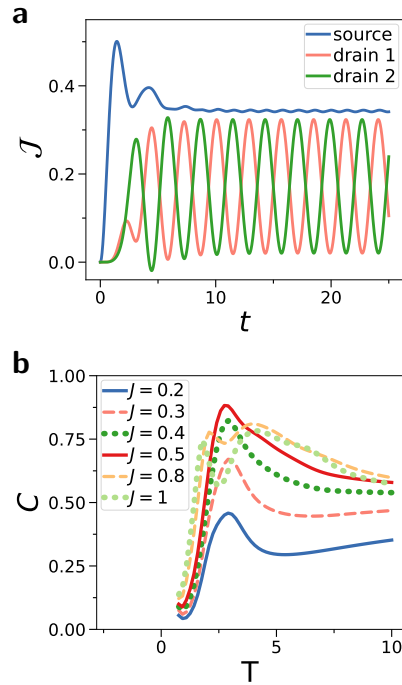


FIG. 5. **a)** Current $\mathcal{J}(t)$ in time t for a linearly increasing flux $\Omega(t) = t/T$ with driving period $T = 2.8$ and $J = \frac{1}{2}$. **b)** DC/AC conversion efficiency $C = \Delta\mathcal{J}_{\text{drain}}/\langle\mathcal{J}_{\text{source}}\rangle$ measured as the drain current amplitude relative to average source current against driving period T of the flux $\Omega(t) = t/T$. We have hard-cores bosons with $L = 3$, $K = 1$, $J = 0.5$ and $B_\alpha = 1$.

we ignore the initial transient dynamics and take the maximum over the long-time behavior $t/T \gg 1$. For $C = 1$ the amplitude of the drain current oscillation matches the source current, implying that the all of the source current is converted from DC to AC. We find that $\Delta\mathcal{J}/\langle\mathcal{J}_{\text{source}}\rangle$ increases sharply with T and reaches a peak around $T = 2.8$ for $J \approx \frac{1}{2}$, then decreases. For $J = 1$ we observe pronounced peaks and dips akin to resonances. For small T , the driving is much faster than the system dynamics which suppresses oscillations. For large T , the current follows the current of the instantaneous steady state as function of Ω (see SM D). We find maximal DC/AC conversion in the regime of intermediate T with $C \approx 0.88$ for $J = 0.5$ and $T = 2.8$.

Discussion.— We propose a multi-functional atomtronic device with a three-terminal ring circuit. In the low energy regime, transport through the device is realized with density waves. The flux controls the conductance of the source-ring interface yielding a maximal current for $\Omega = 0$ and minimal for $\Omega = \frac{1}{2}$. *In particular, by tuning Ω , our setup controls the type of reflection with a crossover from an Andreev-like to a normal one.* This effect opens up a new sensing technique for rotation detection. By carefully measuring the properties of the reflected density wave, the value of flux can be sub-

sequently obtained, with positive reflection indicating a value of flux close to half-integer. In our setup the flux can be read out via the *in-situ* atom density which could be done in a non-destructive manner. We note that for any value of flux both drains have symmetric currents. We believe the phase of the Bose-Einstein condensate interacting with the flux induces this symmetry.

Far from the ground state, the system is characterized by a substantially different dynamics. By analysing both the non-interacting (Landauer formalism) and the strongly interacting systems (Lindblad) dynamics, we can control in which drain the current flows. *By choosing the flux around $\Omega = (2k+1)/4$, k being integer, we find a non-reciprocal behavior where we can direct the flow into either of the drains.* With this effect we can switch the matter-wave between different output terminals to realize a transistor or a rotation sensor.

By sweeping the flux linearly in time, the matter-wave experiences a time-dependent Aharonov-Bohm effect. This could be experimentally achieved by a constant acceleration of the rotation affecting the ring. A linear increase in flux generates a sinusoidal modulation of the current in time. The frequency of the current depends on the periodicity of flux $\Omega \rightarrow \Omega + k$. *As a result, a constant source current is converted into an alternating current in the drains.* The alternating currents of drain 1 and 2 are shifted relative to each other by a phase π . We can control the frequency of the current via the rate change of the flux. We find a near-optimal DC to AC conversion of $C \approx 0.88$ for a the time period $T = 2.8$ and $J = 0.5$. In a reverse operation, this remarkable feature can be used as a sensor for time-dependent rotations $\Omega(t)$. In particular, by measuring the frequency of the current one could read out the acceleration of the rotation.

The time-dependent synthetic flux also allows us to study the time-dependent Aharonov-Bohm effect with cold atoms in a controlled environment, which is a challenging problem in other systems [51–54]. To simulate electrodynamics, the time-dependence of the synthetic flux has to be adjusted to account for induced electric fields. Future studies with cold atoms could help answer the fundamental open question whether there is a time-dependent Aharonov-Bohm effect for charged particles in magnetic fields [51–54].

To our knowledge, we provide the first cold atom system that integrates switch-like and frequency generating capabilities. Our work relies on current experimental capabilities of the field and we experimentally demonstrate the initial setup of our device with a BEC in a light-shaped potential. Our results can be applied in experimental cold atom platforms and help define new applications in atomtronics.

Acknowledgements.— We thank many participants of the Atomtronics conference 2022 in Benasque for fruitful discussions. This work is supported by the Singapore Ministry of Education (MOE) and the Singapore

National Research Foundation (NRF).

* e0032323@u.nus.edu

† On leave from the Dipartimento di Fisica e Astronomia “Ettore Majorana”, University of Catania.

‡ tobias.haug@u.nus.edu

- [1] I. Bloch, J. Dalibard, and S. Nascimbene, Quantum simulations with ultracold quantum gases, *Nature Physics* **8**, 267 (2012).
- [2] M. Keil, O. Amit, S. Zhou, D. Groszwasser, Y. Japha, and R. Folman, Fifteen years of cold matter on the atom chip: promise, realizations, and prospects, *Journal of modern optics* **63**, 1840 (2016).
- [3] L. Amico, D. Anderson, M. Boshier, J.-P. Brantut, L.-C. Kwek, A. Minguzzi, and W. von Klitzing, Atomtronic circuits: from basic research in many-body physics to applications for quantum technologies, *arXiv preprint arXiv:2107.08561* (2021).
- [4] L. Amico, M. Boshier, G. Birk, A. Minguzzi, C. Miniatura, L.-C. Kwek, D. Aghamalyan, V. Ahufinger, D. Anderson, N. Andrei, *et al.*, Roadmap on atomtronics: State of the art and perspective, *AVS Quantum Science* **3**, 039201 (2021).
- [5] L. Amico, G. Birk, M. Boshier, and L.-C. Kwek, Focus on atomtronics-enabled quantum technologies, *New Journal of Physics* **19**, 020201 (2017).
- [6] D. McGloin, G. C. Spalding, H. Melville, W. Sibbett, and K. Dholakia, Applications of spatial light modulators in atom optics, *Optics Express* **11**, 158 (2003).
- [7] C. Ryu and M. G. Boshier, Integrated coherent matter wave circuits, *New Journal of Physics* **17**, 092002 (2015).
- [8] G. Gauthier, I. Lenton, N. M. Parry, M. Baker, M. Davis, H. Rubinsztein-Dunlop, and T. Neely, Direct imaging of a digital-micromirror device for configurable microscopic optical potentials, *Optica* **3**, 1136 (2016).
- [9] D. Barredo, V. Lienhard, S. De Leseleuc, T. Lahaye, and A. Browaeys, Synthetic three-dimensional atomic structures assembled atom by atom, *Nature* **561**, 79 (2018).
- [10] B. Seaman, M. Krämer, D. Anderson, and M. Holland, Atomtronics: Ultracold-atom analogs of electronic devices, *Physical Review A* **75**, 023615 (2007).
- [11] R. Pepino, J. Cooper, D. Anderson, and M. Holland, Atomtronic circuits of diodes and transistors, *Physical review letters* **103**, 140405 (2009).
- [12] R. A. Pepino, Advances in atomtronics, *Entropy* **23**, 534 (2021).
- [13] D. Z. Anderson, Matter waves, single-mode excitations of the matter-wave field, and the atomtronic transistor oscillator, *Physical Review A* **104**, 033311 (2021).
- [14] S. C. Caliga, C. J. Straatsma, A. A. Zozulya, and D. Z. Anderson, Principles of an atomtronic transistor, *New Journal of Physics* **18**, 015012 (2016).
- [15] S. C. Caliga, C. J. Straatsma, and D. Z. Anderson, Transport dynamics of ultracold atoms in a triple-well transistor-like potential, *New Journal of Physics* **18**, 025010 (2016).
- [16] S. C. Caliga, C. J. Straatsma, and D. Z. Anderson, Experimental demonstration of an atomtronic battery, *New Journal of Physics* **19**, 013036 (2017).
- [17] K. W. Wilsmann, L. H. Ymai, A. P. Tonel, J. Links,

and A. Foerster, Control of tunneling in an atomtronic switching device, *Communications physics* **1**, 1 (2018).

[18] C. Ryu, E. Samson, and M. G. Boshier, Quantum interference of currents in an atomtronic squid, *Nature communications* **11**, 1 (2020).

[19] S. Eckel, J. G. Lee, F. Jendrzejewski, N. Murray, C. W. Clark, C. J. Lobb, W. D. Phillips, M. Edwards, and G. K. Campbell, Hysteresis in a quantized superfluid ‘atomtronic’ circuit, *Nature* **506**, 200 (2014).

[20] K. C. Wright, R. Blakestad, C. Lobb, W. Phillips, and G. Campbell, Driving phase slips in a superfluid atom circuit with a rotating weak link, *Physical review letters* **110**, 025302 (2013).

[21] A. Pérez-Obiol, J. Polo, and L. Amico, Coherent phase slips in coupled matter-wave circuits, *arXiv preprint arXiv:2112.08072* (2021).

[22] H. Kiehn, V. P. Singh, and L. Mathey, Implementation of an atomtronic squid in a strongly confined toroidal condensate, *arXiv preprint arXiv:2204.03000* (2022).

[23] C.-C. Chien, S. Peotta, and M. Di Ventra, Quantum transport in ultracold atoms, *Nature Physics* **11**, 998 (2015).

[24] A. J. Heeger, S. Kivelson, J. Schrieffer, and W.-P. Su, Solitons in conducting polymers, *Reviews of Modern Physics* **60**, 781 (1988).

[25] M. Atala, M. Aidelsburger, J. T. Barreiro, D. Abanin, T. Kitagawa, E. Demler, and I. Bloch, Direct measurement of the zak phase in topological bloch bands, *Nature Physics* **9**, 795 (2013).

[26] H. Miyake, G. A. Siviloglou, C. J. Kennedy, W. C. Burton, and W. Ketterle, Realizing the harper hamiltonian with laser-assisted tunneling in optical lattices, *Physical review letters* **111**, 185302 (2013).

[27] M. Aidelsburger, M. Atala, M. Lohse, J. T. Barreiro, B. Paredes, and I. Bloch, Realization of the hofstadter hamiltonian with ultracold atoms in optical lattices, *Physical review letters* **111**, 185301 (2013).

[28] G. Jotzu, M. Messer, R. Desbuquois, M. Lebrat, T. Uehlinger, D. Greif, and T. Esslinger, Experimental realization of the topological haldane model with ultracold fermions, *Nature* **515**, 237 (2014).

[29] J.-P. Brantut, J. Meineke, D. Stadler, S. Krinner, and T. Esslinger, Conduction of ultracold fermions through a mesoscopic channel, *Science* **337**, 1069 (2012).

[30] S. Krinner, D. Stadler, D. Husmann, J.-P. Brantut, and T. Esslinger, Observation of quantized conductance in neutral matter, *Nature* **517**, 64 (2015).

[31] D. Husmann, S. Uchino, S. Krinner, M. Lebrat, T. Giamarchi, T. Esslinger, and J.-P. Brantut, Connecting strongly correlated superfluids by a quantum point contact, *Science* **350**, 1498 (2015).

[32] M. Lebrat, P. Grisins, D. Husmann, S. Häusler, L. Corman, T. Giamarchi, J.-P. Brantut, and T. Esslinger, Band and correlated insulators of cold fermions in a mesoscopic lattice, *Physical Review X* **8**, 011053 (2018).

[33] G. Gauthier, S. S. Szigeti, M. T. Reeves, M. Baker, T. A. Bell, H. Rubinsztein-Dunlop, M. J. Davis, and T. W. Neely, Quantitative acoustic models for superfluid circuits, *Phys. Rev. Lett.* **123**, 260402 (2019).

[34] S. Pandey, H. Mas, G. Drougakis, P. Thekkepatt, V. Bolpasi, G. Vasilakis, K. Poulios, and W. von Klitzing, Hypersonic bose-einstein condensates in accelerator rings, *Nature* **570**, 205 (2019).

[35] T. Haug, L. Amico, R. Dumke, and L.-C. Kwek, Mesoscopic vortex-meissner currents in ring ladders, *Quantum Science and Technology* **3**, 035006 (2018).

[36] T. Haug, R. Dumke, L.-C. Kwek, and L. Amico, Topological pumping in aharonov-bohm rings, *Communications Physics* **2**, 1 (2019).

[37] T. Haug, H. Heimonen, R. Dumke, L.-C. Kwek, and L. Amico, Aharonov-bohm effect in mesoscopic bose-einstein condensates, *Physical Review A* **100**, 041601 (2019).

[38] S. Safaei, L.-C. Kwek, R. Dumke, and L. Amico, Monitoring currents in cold-atom circuis, *Physical Review A* **100**, 013621 (2019).

[39] T. Haug, R. Dumke, L.-C. Kwek, and L. Amico, Andreev-reflection and aharonov-bohm dynamics in atomtronic circuits, *Quantum Science and Technology* **4**, 045001 (2019).

[40] T. F. Haug, *Quantum transport with cold atoms*, Ph.D. thesis, National University of Singapore (Singapore) (2021).

[41] A. Ramanathan, K. Wright, S. R. Muniz, M. Zelan, W. Hill III, C. Lobb, K. Helmerson, W. Phillips, and G. Campbell, Superflow in a toroidal bose-einstein condensate: an atom circuit with a tunable weak link, *Physical review letters* **106**, 130401 (2011).

[42] C. Ryu, P. Blackburn, A. Blinova, and M. Boshier, Experimental realization of josephson junctions for an atom squid, *Physical review letters* **111**, 205301 (2013).

[43] B. Eller, O. Oladehin, D. Fogarty, C. Heller, C. W. Clark, and M. Edwards, Producing flow in racetrack atom circuits by stirring, *Physical Review A* **102**, 063324 (2020).

[44] D. Aghamalyan, M. Cominotti, M. Rizzi, D. Rossini, F. Hekking, A. Minguzzi, L.-C. Kwek, and L. Amico, Coherent superposition of current flows in an atomtronic quantum interference device, *New journal of Physics* **17**, 045023 (2015).

[45] T. Haug, J. Tan, M. Theng, R. Dumke, L.-C. Kwek, and L. Amico, Readout of the atomtronic quantum interference device, *Physical Review A* **97**, 013633 (2018).

[46] Y. Aharonov and D. Bohm, Significance of electromagnetic potentials in the quantum theory, *Physical Review* **115**, 485 (1959).

[47] Y. Gefen, Y. Imry, and M. Y. Azbel, Quantum oscillations and the aharonov-bohm effect for parallel resistors, *Physical review letters* **52**, 129 (1984).

[48] M. Büttiker, Y. Imry, and M. Y. Azbel, Quantum oscillations in one-dimensional normal-metal rings, *Physical Review A* **30**, 1982 (1984).

[49] R. A. Webb, S. Washburn, C. Umbach, and R. Laibowitz, Observation of h e aharonov-bohm oscillations in normal-metal rings, *Physical Review Letters* **54**, 2696 (1985).

[50] Y. Imry, *Introduction to mesoscopic physics*, 2 (Oxford University Press on Demand, 2002).

[51] D. Singleton and E. C. Vagenas, The covariant, time-dependent aharonov-bohm effect, *Physics Letters B* **723**, 241 (2013).

[52] J. Macdougall, D. Singleton, and E. C. Vagenas, Revisiting the marton, simpson, and suddeth experimental confirmation of the aharonov-bohm effect, *Physics Letters A* **379**, 1689 (2015).

[53] J. Jing, Y.-F. Zhang, K. Wang, Z.-W. Long, and S.-H. Dong, On the time-dependent aharonov-bohm effect, *Physics Letters B* **774**, 87 (2017).

[54] S. R. Choudhury and S. Mahajan, Direct calculation of time varying aharonov-bohm effect, *Physics Letters A*

383, 2467 (2019).

[55] D. Jaksch and P. Zoller, Creation of effective magnetic fields in optical lattices: the hofstadter butterfly for cold neutral atoms, *New Journal of Physics* **5**, 56 (2003).

[56] Y.-J. Lin, R. L. Compton, K. Jiménez-García, J. V. Porto, and I. B. Spielman, Synthetic magnetic fields for ultracold neutral atoms, *Nature* **462**, 628 (2009).

[57] J. Dalibard, F. Gerbier, G. Juzeliūnas, and P. Öhberg, Colloquium: Artificial gauge potentials for neutral atoms, *Reviews of Modern Physics* **83**, 1523 (2011).

[58] T. Haug, R. Dumke, L.-C. Kwek, C. Miniatura, and L. Amico, Machine-learning engineering of quantum currents, *Physical Review Research* **3**, 013034 (2021).

[59] G. Del Pace, K. Xhani, A. M. Falconi, M. Fedrizzi, N. Grani, D. H. Rajkov, M. Inguscio, F. Scazza, W. Kwon, and G. Roati, Imprinting persistent currents in tunable fermionic rings, *arXiv preprint arXiv:2204.06542* (2022).

[60] P. Engels, I. Coddington, P. Haljan, V. Schweikhard, and E. A. Cornell, Observation of long-lived vortex aggregates in rapidly rotating bose-einstein condensates, *Physical review letters* **90**, 170405 (2003).

[61] C. Weitenberg and J. Simonet, Tailoring quantum gases by floquet engineering, *Nature Physics* **17**, 1342 (2021).

[62] M. Fishman, S. R. White, and E. M. Stoudenmire, The ITensor software library for tensor network calculations, *arXiv:2007.14822* (2020).

[63] H.-P. Breuer, F. Petruccione, *et al.*, *The theory of open quantum systems* (Oxford University Press on Demand, 2002).

[64] C. Guo and D. Poletti, Dissipatively driven hardcore bosons steered by a gauge field, *Physical Review B* **96**, 165409 (2017).

[65] R. Landauer, Spatial variation of currents and fields due to localized scatterers in metallic conduction, *IBM Journal of research and development* **1**, 223 (1957).

[66] R. Landauer, Electrical resistance of disordered one-dimensional lattices, *Philosophical magazine* **21**, 863 (1970).

[67] R. Landauer, Electrical transport in open and closed systems, *Zeitschrift für Physik B Condensed Matter* **68**, 217 (1987).

[68] B. Kramer, G. Bergmann, and Y. Bruynseraede, *Localization, Interaction, and Transport Phenomena: Proceedings of the International Conference, August 23–28, 1984 Braunschweig, Fed. Rep. of Germany*, Vol. 61 (Springer Science & Business Media, 2012).

[69] B. Shapiro, Quantum conduction on a cayley tree, *Physical Review Letters* **50**, 747 (1983).

Appendix A: Landauer formula

The Landauer formula [65–68] is used in mesoscopic systems to express the conductance in terms of the scattering properties of the geometry of the problem. It is a useful tool to study transport properties and obtain exact expressions for the transport properties of quantum conductors. It has the advantage over semiclassical transport theories that it captures interference phenomena in the conductance. It has been used to calculate the conductance for rings subject to a flux [47, 48]. The formalism expresses branches and junctions in terms of scattering matrices. The geometry of the system we are considering is shown in Fig. 6.

We model the ring as single-channel conductors connecting the branches between the three junctions to the source and drain leads. Each such branch is described as a single scatterer connected to an ideal one-dimensional channel. The scattering can be described with a 2×2 scattering matrix

$$\mathcal{S}_j = \begin{bmatrix} r_j & t_j \\ t'_j & r'_j \end{bmatrix}. \quad (\text{A1})$$

All phases and scattering effects that occur within each branch are absorbed into the parameters of the scattering matrix. In the absence of flux through the ring, time-reversal and current-conservation (demanding unitarity) impose the following constraints on the scattering matrix: $t_j = t'_j$ and $-t_j/(t'_j)^* = r_j/(r'_j)^*$. To account for the flux which breaks time-reversal symmetry, we use the Peierls substitution $t_j \rightarrow t_j e^{-i2\pi\Omega/3}$, $t'_j \rightarrow t_j e^{i2\pi\Omega/3}$, $r_j \rightarrow r_j$, $r'_j \rightarrow r'_j$. The prior constraints on t_j, r_j and r'_j remain the same such that we obtain valid scattering matrices. For the \mathcal{S}_1 arm, we get a system of equations that describe the scattering in this arm

$$\begin{bmatrix} B \\ C \end{bmatrix} = \begin{bmatrix} r_1 & t_1 e^{-i2\pi\Omega/3} \\ t_1 e^{i2\pi\Omega/3} & r'_1 \end{bmatrix} \begin{bmatrix} A \\ D \end{bmatrix}. \quad (\text{A2})$$

We can model the junctions that connect to the leads with a 3×3 scattering matrix \mathcal{U} [69]

$$\mathcal{U} = \begin{bmatrix} 0 & -\frac{1}{\sqrt{2}} & -\frac{1}{\sqrt{2}} \\ -\frac{1}{\sqrt{2}} & \frac{1}{2} & -\frac{1}{2} \\ -\frac{1}{\sqrt{2}} & -\frac{1}{2} & \frac{1}{2} \end{bmatrix}. \quad (\text{A3})$$

The first channel is the path leading out of the ring to one of the leads. \mathcal{U} describes a scenario where there is no instantaneous reflection for particles entering the ring from the channel and we can scatter in both directions in the

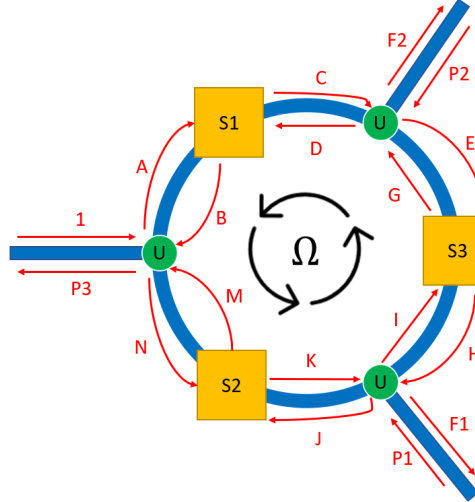


FIG. 6. Three-terminal ring device described with Landauer formula. The left channel represents the path towards the source lead, while the top and bottom right channels represent the path towards the two drains. The arms of the ring are represented by scattering matrices \mathcal{S}_1 , \mathcal{S}_2 and \mathcal{S}_3 , and the flux is absorbed into their parameters via the Peierls substitution. The junctions connecting ring to source and drains are represented by the scattering matrix \mathcal{U} .

ring with equal probability. While the scattering matrix \mathcal{U} that fulfils these conditions is not unique, the results do not qualitatively depend on the specific choice of \mathcal{U} .

We solve the equations by writing down the relationships between the various amplitudes at the junctions and scatterers. We demand that the channel of the source lead into the ring is unitary and setting that P_1 and P_2 is zero, which means that particles that exit to the drains cannot return. As a result, we get a linear system of 15 equations and 15 unknowns. We solve it for F_1 and F_2 which are the complex amplitudes of the transmission into the respective drains. Then, we insert the values for all the scattering coefficients t_j , r_j and r'_j .

The final result depends on how we choose these scattering coefficients as they determine the transport properties of the ring. From physical consideration, we demand that transmission and reflection occur with equal probability and we demand that clockwise and anti-clockwise reflection is the same $r_j = r'_j$. These considerations lead us to the choice $r_j = r'_j = \sqrt{1/2}$ and $t_j = i\sqrt{1/2}$.

The transmission $G_\alpha = |F_\alpha|^2$ into the respective drains $\alpha \in \{0, 1\}$ is then given by

$$G_\alpha = 16 \left| \frac{1 - \sqrt{2} + 2i(2\sqrt{2} - 3) \exp(-i\pi(2\Omega + \alpha))}{62 - 46\sqrt{2} + 2i \cos(\pi(2\Omega + \alpha))} \right|^2. \quad (\text{A4})$$

As seen in the main text, the transmission strongly depends on the flux Ω and can be tuned to maximize transmission into a particular drain.

Appendix B: Flux dependence of dynamics close to ground state

Here, we show further results on the dynamics in the three terminal device close to the ground state. We prepare a density perturbation in the source, then quench the Hamiltonian and create a propagating density wave. The dynamics of the change of density in time for different values of flux is shown in Fig.7. The perturbation starts from the source and moves both forward and backward in sites. The backward propagating wave stays in the source within our simulation time, and is simply reflected at the other end of the source. It has no influence on the rest of the system and can be ignored. The forward moving density wave propagates through the ring, where it is both transmitted into the drains, as well as reflected back into the source. For $\Omega = 0$, we find a negative Andreev reflection, whereas for $\Omega = 0.5$, we find a clear positive reflection.

The dynamics is periodic with $\Omega \rightarrow \Omega + k$, where k is an integer. Note that $\Omega = 0.25 + k$ and $\Omega = 0.75 + k$ produces nearly the same dynamics, demonstrating a reflection symmetry $\Omega \rightarrow -\Omega$ for the dynamics close to the ground state.

For any value of flux, we observe that the current into drain 1 and drain 2 is nearly identical. Both the reflection symmetry and the symmetry in the drains is a low-energy effect that is absent for the strongly perturbed dynamics.

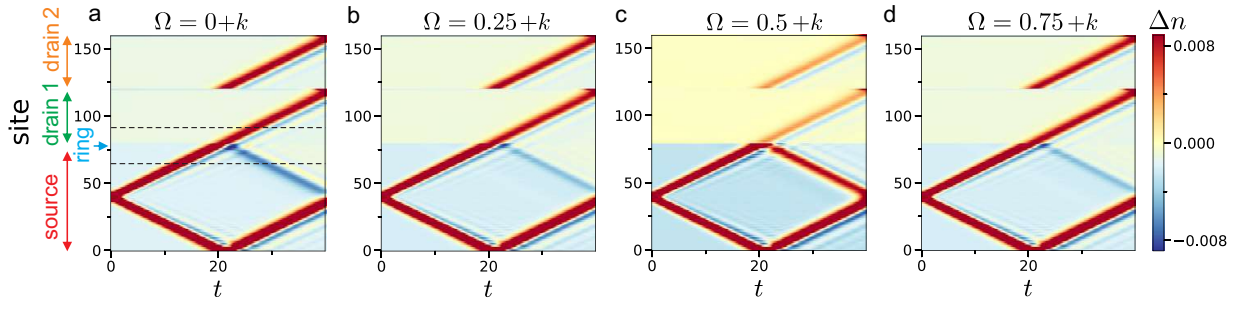


FIG. 7. Dynamics of density wave in three-terminal device. **a)** Change of density relative to average density $\Delta n(t) = \langle n(t) \rangle - n_0$ as function of time and sites of source, ring, drain 1 and 2. We show **a)** $\Omega = k$ **b)** $\Omega = 0.25 + k$, **c)** $\Omega = 0.5 + k$ and **d)** $\Omega = 0.75 + k$, where k is an integer. Perturbation starts in source, and moves through ring into drains. Note that the dynamics in both drains is symmetric for all values of flux. We have hard-core bosons with $J = 1$, $K = 0.5$ and in total $L = 160$ lattice sites and $N = 80$ bosons ($L = 3$, $L_s = 79$, $L_b = L_c = 39$).

Appendix C: Non-equilibrium dynamics

Here we provide further results on the non-equilibrium dynamics. In Fig.8a,b we show the steady-state current through source and drains as function of flux Ω . The current in drain 1 and 2 varies strongly with Ω , allowing for directional control into either drain. For the source current, we find for $J = 0.5$ in Fig.8a no variation with Ω , whereas for $J = 1$ the current in source varies strongly (Fig.8b). In Fig.8c, we investigate the current as function of intra-ring coupling J . The solid blue line shows the mean drain current $\langle J_{\text{drain}} \rangle$ averaged over Ω . The dashed orange line is the maximal difference between the two drain currents $\Delta J_{\text{drains}} = \max_{\Omega} (|J_{\text{drain } 1}(\Omega) - J_{\text{drain } 2}(\Omega)|)$. The dotted green curve is the amplitude of the source current $\Delta J_{\text{source}} = \max_{\Omega} J_{\text{source}} - \min_{\Omega} J_{\text{source}}$. We find a transition from $\Delta J_{\text{source}} \approx 0$ to $\Delta J_{\text{source}} \gtrsim 0$ for $J > 0.5$. Further, the amplitude and mean value of the drain current shows a peak at the transition $J \approx 0.5$. This indicates that our system features a non-equilibrium transition in the flux dependence of the current.

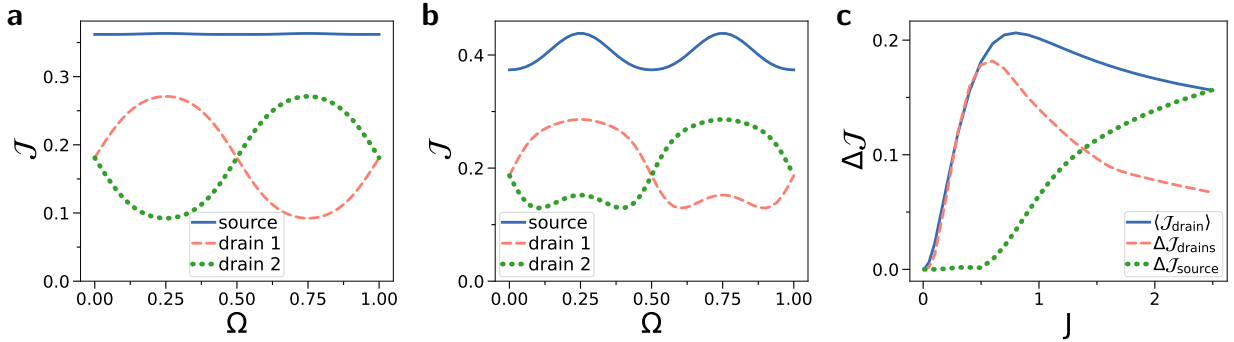


FIG. 8. Steady-state current J for hard-core bosons as function of flux Ω for **a)** $J = 0.5$ **b)** $J = 1$. **c)** Mean value of drain current $\langle J_{\text{drain}} \rangle$ taken over Ω , maximal difference between drain 1 and drain 2 current $\Delta J_{\text{drains}} = \max_{\Omega} (|J_{\text{drain } 1}(\Omega) - J_{\text{drain } 2}(\Omega)|)$ and amplitude of source current $\Delta J_{\text{source}} = \max_{\Omega} J_{\text{source}} - \min_{\Omega} J_{\text{source}}$ as function of intra-ring coupling J . We set $L = 3$, $K = 1$ and $B_s = B_d = 1$.

Appendix D: Time-dependent flux

We show further results on driving the flux of the ring linearly in time in Fig.7. For very fast driving $T = 1$ in Fig.7a, we find that the current shows barely any oscillation as the driving is much faster than the system dynamics.

For intermediate driving $T = 2.8$ in Fig.7b, we find strong oscillations. The amplitude of the drain currents is nearly the same as the source current, implying that most of the incoming direct current is converted into an alternating current. For very slow driving $T \gg 1$ in Fig.7c, the system dynamics is much faster than the driving. Thus, the system has sufficient time to settle into the instantaneous steady state of the flux. The current then simply takes the same value as the current of the steady state of the system $\rho_{\text{ss}}(\Omega(t))$ at a given flux $\Omega(t)$.

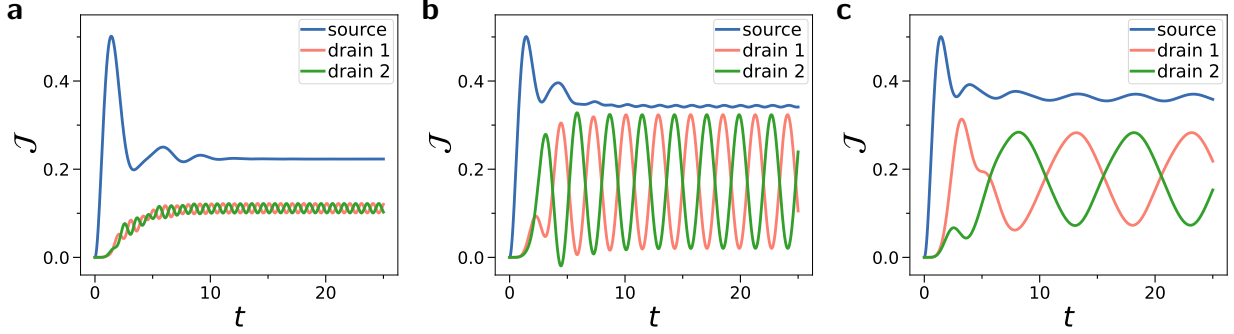


FIG. 9. Current $J(t)$ in time t for various driving periods T of the flux $\Omega(t) = t/T$ for **a)** $T = 1$, **b)** $T = 2.8$ and **c)** $T = 10$. We have $L = 3$, $K = 1$, $J = 0.5$ and $B_s = B_d = 1$.

Appendix E: Experimental details

Here we give details on the experimental demonstration of the Bose-Einstein condensate in the potential of a three-terminal ring as shown in Fig.1b.

The experiment starts with a Magneto-Optical Trap (MOT) which traps up to 7×10^8 Rubidium 87 atoms with a temperatures of $20\mu\text{K}$ for 5ms. Magnetic field biases with an optical pump beam pumps the atoms into the $F = 2, m_f = +2$ state. A magnetic field gradient of 220G/cm is then ramped up in 150ms to trap up to 3×10^8 atoms. A 2 second translation stage brings the atoms to a second magnetic trap with lower vacuum pressure. Due to heating processes during this step, a Radio-Frequency (RF) evaporative cooling step is then further performed to condense the atoms back to $20\mu\text{K}$. An atom cloud of 1×10^7 atoms remains after this step. At the same time, a 1064nm laser beam for optical trapping of the atoms is ramped up to 5W, and subsequently a ramp down of the MOT is performed, leaving behind a pure optical trap.

Next, an optical evaporation step is performed. The laser power is first lowered from 9.0V to 6.0V in 2s, where the atom temperature reaches $1\mu\text{K}$ and the atom number is 1×10^6 . The second ramp brings the voltage from 6.0V to 5.0V in 3s with a temperature of 250nK and atom number 3.5×10^5 .

The final ramp occurs in 2s from 5.0V to 4.8V where we get a Bose-Einstein condensate (BEC) of 1.8×10^5 atoms with a phase space density of 3.0. The optical setup for creating arbitrary traps in 2D comprises a Digital Micromirror Device (DMD) setup and an optical sheet. The DMD (DLP9500) has dimensions of 20.7mm x 11.7mm with pitch of $10.8\mu\text{m}$. A controller board (V4395) from Texas Instruments controls the operation of the DMD. We draw the potential of the ring with the three leads by electronically controlling the mirror array of the DMD. The drawn ring has a outer radius of $R_1 = 15\mu\text{m}$, an inner radius of $R_0 = 9\mu\text{m}$, and the center of the ring has a radius of $R = 12\mu\text{m}$. A blue-detuned (532nm) 10mm beam diameter is reflected off the DMD with 40% efficiency in the first order with all mirrors on. This beam is first de-magnified 4 times with a 300mm-75mm lens configuration, and later 20 times with a 200mm-20x objective (Mitutoyo M Plan APO NIR 20x, NA = 0.40) for a total of 80x de-magnification. The 1st order beam at the atom plane has a maximum 190mW of beam power at a beam radius of $62.5\mu\text{m}(1/e^2)$ giving a maximum trap depth of $1.8\mu\text{K}$. Utilising the same objective lens, a dichroic mirror reflects the absorption image of the atoms through a 200mm lens and imaged onto an ANDOR EMCCD. The resonant imaging beam is delivered from below the atoms with a pulse time of 10 μs to minimise the force on the atoms. The optical sheet for 2D trapping is generated via intersecting 2 beams using a single lens. The interference of the 2 beams creates optical sheets superimposed on the beam profile. Our beam is asymmetric at the focus with 50 μm radius in the vertical direction and 150 μm in the horizontal direction. This minimises the probability of loading into multiple sheets as the interfering beams are static. The interfering beams are distanced such that the interference sheets are spaced 7.5 μm apart.

Loading of a BEC into the combined blue-detuned trap starts with a BEC at 50% purity in the red-detuned crossed

dipole trap. The desired trap is first projected on the DMD, and within 100ms both the DMD and optical sheet are ramped up while keeping the red-detuned trap on. The DMD beam is ramped up to half power while the sheet is ramped up to 63mW per interfering beam. The red-detuned trap is ramped down to a negligible trap depth in 10ms to complete the transfer. The transfer efficiency of the atoms heavily depends on the size of the DMD trap as compared to the initial BEC size. A DMD square trap of side 40 μ m gives a loading efficiency of 50%. The condensation of the BEC in the DMD is verified by observing in the time-of-flight images an asymmetric cloud in the direction perpendicular to the sheet.